



**HAL**  
open science

# Self-heating of metastable 304L austenitic stainless steel under cyclic loading: Influence of initial martensite volume fraction, testing temperature and pre-strain

Behnaz Amini, Younes Demmouche, Mahmoud Barati, Guillaume Helbert, Shabnam Arbab-Chirani, Sylvain Calloch

## ► To cite this version:

Behnaz Amini, Younes Demmouche, Mahmoud Barati, Guillaume Helbert, Shabnam Arbab-Chirani, et al.. Self-heating of metastable 304L austenitic stainless steel under cyclic loading: Influence of initial martensite volume fraction, testing temperature and pre-strain. *Mechanics of Materials*, 2020, 151, pp.103596-1 - 103596-14. 10.1016/j.mechmat.2020.103596 . hal-03127058

**HAL Id: hal-03127058**

**<https://ensta-bretagne.hal.science/hal-03127058>**

Submitted on 17 Oct 2022

**HAL** is a multi-disciplinary open access archive for the deposit and dissemination of scientific research documents, whether they are published or not. The documents may come from teaching and research institutions in France or abroad, or from public or private research centers.

L'archive ouverte pluridisciplinaire **HAL**, est destinée au dépôt et à la diffusion de documents scientifiques de niveau recherche, publiés ou non, émanant des établissements d'enseignement et de recherche français ou étrangers, des laboratoires publics ou privés.



Distributed under a Creative Commons Attribution - NonCommercial 4.0 International License

## Self-heating of metastable 304L austenitic stainless steel under cyclic loading: influence of initial martensite volume fraction, testing temperature and pre-strain

Behnaz Amini<sup>a</sup>, Younes Demmouche<sup>b</sup>, Mahmoud Barati<sup>a</sup>, Guillaume Helbert<sup>a</sup>,  
Shabnam Arbab Chirani<sup>a\*</sup>, Sylvain Calloch<sup>b</sup>

<sup>a</sup> *Ecole Nationale d'Ingénieurs de Brest, ENIB, UMR CNRS 6027, IRDL, F-29200 Brest, France*

<sup>b</sup> *Ecole Nationale Supérieure de Techniques Avancées Bretagne, ENSTA Bretagne, UMR CNRS 6027, IRDL, F-29200 Brest, France*

### ABSTRACT

In this study, special attention is paid to the thermal response of the austenitic stainless steel 304L under cyclic loading tests (i.e., self-heating tests) in different conditions. The cyclic behavior of the 304L austenitic stainless steel can be influenced by martensitic transformation. Hence, the role of martensitic transformation in the self-heating behavior of this material is studied. For this purpose, self-heating tests are performed on pre-strained specimens at a wide range of temperatures from 100°C to -130°C, which leads to different initial volume fractions of martensite ranging from 0% to 45%, respectively. Furthermore, the influence of the testing temperature and a pre-strain at room temperature on the self-heating curves is investigated. The results demonstrate that the decrease in the test temperature from room temperature to -30°C as well as the increase in the pre-strain values from 0% to 30% at room temperature, result in a shift of the self-heating curves to the right. It could mean that the fatigue limit of the material is improved.

Keywords: self-heating under cyclic loading, metastable austenitic stainless steel, martensitic transformation, pre-strain

### 1. Introduction

Austenitic stainless steel materials have found a wide range of applications due to their interesting properties such as high ductility, good corrosion resistance, low cost, easy machining and plentiful supply. In metastable austenitic stainless steels,  $\gamma$ -austenite (FCC) can transform into  $\alpha'$ -martensite (BCC) and/or  $\epsilon$ -martensite (HCP) under the transformation-induced plasticity (TRIP) effect (Pessoa et al., 2017), (Christ et al., 2015). Therefore, the mechanical properties of these materials are significantly affected by deformation-induced martensitic transformation. By applying stress or plastic deformation,

---

\* Corresponding author: shabnam.arbab@enib.fr

austenitic stainless steel can experience phase transformations through three different paths: the first two are that  $\gamma$ -austenite can transform directly into  $\varepsilon$ -martensite or  $\alpha'$ -martensite, and the third is indirect transformation from  $\gamma$  to  $\varepsilon$  and afterwards  $\alpha'$ -martensite (Liu and Kaoumi, 2018). Depending on the value of the stacking fault energy (SFE), martensite can form directly or indirectly. For low SFE values ( $< 18$  mJ/m<sup>2</sup>), indirect transformation ( $\gamma \rightarrow \varepsilon \rightarrow \alpha'$ ) occurs since formation of  $\varepsilon$ -martensite is easier in this case, while high SFE ( $> 18$  mJ/m<sup>2</sup>) causes direct transformation ( $\gamma \rightarrow \alpha'$ ) (Allain et al., 2004; Kaoumi and Liu, 2018; Talonen and Hänninen, 2007). The value of SFE depends on the chemical composition, elastic strain, temperature and magnetic contribution (Talonen and Hänninen, 2007), (Wan et al., 2001).  $\alpha'$ -martensite possesses a higher strength than  $\varepsilon$ -martensite (Christ et al., 2015) and its existence can improve the material properties such as yield stress and fatigue limit.

As martensitic transformation is one of the main parameters that can affect the fatigue behavior of austenitic stainless steel, its effect should be taken into account. Although, a considerable amount of research has been carried out on the fatigue life of this material during the last 25 years (Colin et al., 2010; Gupta et al., 2018; Kamaya and Kawakubo, 2015; Le Roux et al., 2008; Liu et al., 2018; Müller-Bollenhagen et al., 2010a; Nakajima et al., 2007; Paquet et al., 2014; Vincent et al., 2012), the influence of phase transformation on [high cycle fatigue behavior has been examined to a lesser extent](#) (Wu and Huang, 2015; Zeng and Yuan, 2017).

Since, the traditional methods for fatigue characterization are extremely time consuming and costly, several alternative methods have been developed to allow a fast assessment of fatigue properties [such as the ultrasonic fatigue test](#) (Bortoluci Ormastroni et al., 2020; Grigorescu et al., 2016; Torabian et al., 2017) [and other methods](#) (Charkaluk and Constantinescu, 2009; Dengel and Harig, 1980; Doudard et al., 2005; Meneghetti et al., 2016; Ricotta et al., 2019; Risitano and Risitano, 2013). One of the most robust methods for fast evaluation of the fatigue properties of different materials is the self-heating (SH) test, which is based on the assessment of the material temperature variations that occur under cyclic loadings. Since, cyclic loading is an energy-dissipating mechanism, it is accompanied by a rise in temperature in the material. The SH method is based on the measurement of the temperature elevation at the surface of the specimen as a result of the [intrinsic](#) dissipation due to the microplasticity phenomenon (Munier et al., 2017). In this method, successive cyclic loading tests are performed with increasing stress amplitudes

and the temperature evolution relevant to each stress amplitude is registered. Finally, the SH curve is obtained by plotting stabilized mean temperature (which is determined for each loading block) versus stress amplitude. This method allows the endurance limit of a material to be determined using only one sample and a couple of hours of testing, instead of weeks or even months of tests using a considerable amount of samples in order to complete an S-N fatigue curve. The SH method has proved to be an efficient, fast technique for determining the fatigue endurance limit of different alloys such as steels (Krapez, J.-C., Pacou, 2002; Krapez et al., 2000; Louge, 2019; Munier et al., 2014, 2010), titanium TA6V (Roué et al., 2018), chrome-cobalt (Doudard and Calloch, 2009), aluminum 7010, 2024 (Krapez, J.-C., Pacou, 2002) and A7N01 (Zhang et al., 2013), copper–aluminum (Ezanno et al., 2013), shape memory alloys (SMAs) (Mostofizadeh et al., 2019), composites (Abello et al., 2013) and elastomers (Masquelier et al., 2015). However, it has not yet been applied to materials with irreversible phase transformation such as metastable austenitic stainless steels, which would experience a martensitic transformation under thermomechanical loadings.

In the case of austenitic stainless steel, phase transformation can influence fatigue behavior and the SH measurements can contribute to a better understanding of simultaneous microplasticity and martensitic transformation mechanisms during cyclic loading. For other materials that experience phase transformation such as SMAs, the predicted endurance limit using the self-heating method is in good agreement with the results obtained by classic fatigue tests (Mostofizadeh et al., 2019). This fact is encouraging considering the complexity of martensitic transformation. Nevertheless, unlike SMAs, martensitic transformation is irreversible in the context of metastable austenitic stainless steels. However, the capability of the SH method to predict the fatigue limit of austenitic stainless steel should be investigated as it is not in the scope of this paper.

This study focuses on the SH response of the austenitic stainless steel 304L and the effect of different parameters and initial states of the material on SH curves is investigated. As far as we are aware, there is no study in the literature about SH and high cycle fatigue behavior of this material at low temperatures, which reflects the importance of this study. This paper is subdivided into three main parts. Firstly, the mechanical behavior of the studied material at different temperatures ranging from -130°C to 100°C is determined. In the second part, the SH test procedure and underlying assumptions of the OD approach

details are fully explained. In addition, the effect of different parameters such as (i) the testing temperature, (ii) the pre-strain (PS) at room temperature (RT) and (iii) the initial volume fractions of martensite (VFM) are examined. This pre-existing martensite can affect the yield stress as well as the SH behavior of the material. It is worth noting that this is the first time that the effect of VFM on SH behavior is decoupled from its effect on yield stress. Finally, microstructural observations are performed using FERITSCOPE, scanning electron microscopy (SEM) and electron backscatter diffraction (EBSD) to determine the different initial states of the material as well as the microstructural evolutions after SH tests.

## 2. Material specifications

### 2.1. Studied material

The material examined in this study is 304L austenitic stainless steel. The chemical composition of this material is given in Table 1.

Table 1. Chemical composition of stainless steel 304L (wt. %)

C	Mn	P	S	Si	Cr	Ni	N	Mo	Cu	Iron
0.029	1.89	0.028	0.001	0.33	18.20	9.32	0.08	0.26	0.28	Balance

Based on the chemical composition, there are multiple empirical formulas to estimate the austenite stability via specific parameters such as the martensite start temperature ( $M_s$ ) and the SFE. The values calculated for the  $M_s$  and SFE using various equations from the literature (Hahnenberger et al., 2014; Schramm and Reed, 1975; Smaga et al., 2006) are about  $-181^\circ\text{C}$  and  $26 \text{ mJ/m}^2$ , respectively.

To prepare the specimens, cylinders of 30 mm diameter were extracted from bulk material by water jet cutting. Before machining, in order to eliminate the internal stresses and the history effects due to the manufacturing process, these cylinders were annealed at  $T=1050^\circ\text{C}$  for 10 minutes using argon gas and then, quenched in water. After this heat treatment, the material becomes pure austenite (Christ et al., 2015). Figure 1 shows a homogeneous and purely austenitic microstructure. This microstructure consists of polygonal austenitic grains with some [annealing](#) twins. The average grain size of the heat-treated material is about 100-150  $\mu\text{m}$ .

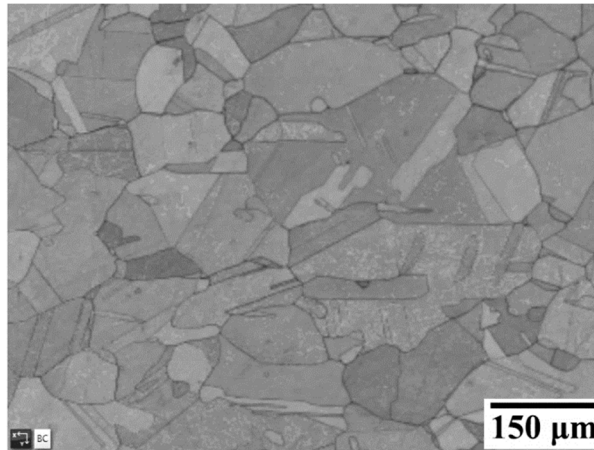


Fig. 1. Microstructure of heat-treated material

The heat-treated cylinders were then machined to obtain the final shape of the specimens. This specimen shape was designed to allow the use of mechanical fixtures in the thermal chambers and to apply tension-compression loadings. The specimen geometry is depicted in Figure 2.

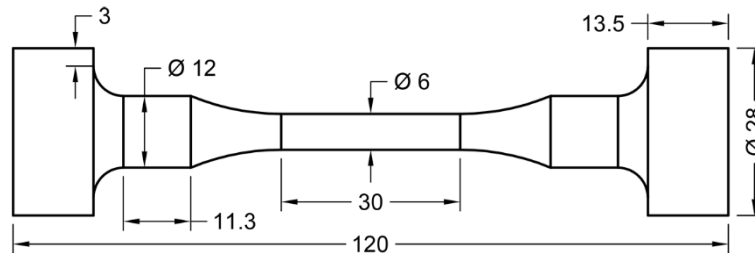


Fig. 2. Specimen geometry (dimensions in mm)

## 2.2. Experimental setup

Uniaxial tensile and SH tests were carried out using a servo-hydraulic traction-torsion-compression (TTC) machine with a load capacity of  $\pm 100$  kN. The strain was measured by an Epsilon axial extensometer with a gauge length of 25 mm and a working temperature range of between  $-270^{\circ}\text{C}$  and  $100^{\circ}\text{C}$ . Moreover, to measure the temperatures, three T-type thermocouples were taped onto the center of the sample and the lower and the upper jaws of the testing machine.

To conduct the tests at different temperatures using the thermal chambers, special jaws were designed enabling the application of tension-compression loading. An electrical thermal chamber was used to perform the tests at temperatures ranging from  $-50^{\circ}\text{C}$  to  $100^{\circ}\text{C}$  and a cryogenic chamber fed by liquid nitrogen was employed for lower temperatures down to  $-130^{\circ}\text{C}$ . This experimental setup is shown in Figure 3.

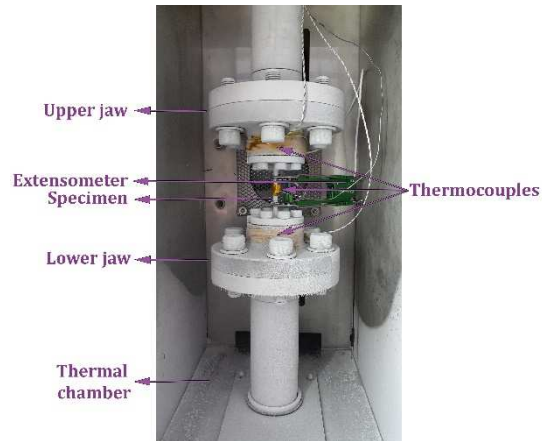


Fig. 3. Experimental setup for the controlled environment temperature tests

For microstructural observations, a JEOL JSM-IT300LV Scanning Electron Microscope (SEM) equipped with Nordlys detectors was used. The Electron Back-Scattered Diffraction (EBSD) measurements were performed on an AZTEC system provided by OXFORD Instruments. EBSD was carried out at two different magnifications of  $150\times$  and  $350\times$  and the step size chosen for each magnification was of  $0.7\ \mu\text{m}$  and  $0.5\ \mu\text{m}$ , respectively. In addition, the number of grains analyzed was about 80. Three different areas through the gauge length (one area in the middle and two others near the border of the gauge length) were scanned for each specimen to improve the statistical analysis. EBSD analysis was used to identify the phase fractions and their distribution on the one hand and to determine the crystallographic orientations and morphology on the other hand.

For EBSD analysis, samples need meticulous preparation. The samples were mechanically polished through different steps, finishing with an oxide polishing suspension (OP-S) up to  $0.04\ \mu\text{m}$ .

The ferrite content was measured using a FERITSCOPE FMP30, which is based on the magnetic induction method. By this method, paramagnetic austenite can be separated from ferromagnetic  $\alpha'$ -martensite. Since the FERITSCOPE was calibrated to measure the ferrite content, it was necessary to convert these magneto-inductive values to  $\alpha'$ -martensite. A multiplication factor was identified in accordance with (Müller-Bollenhagen et al., 2010a; Talonen et al., 2004) by fitting the results obtained and the VFM determined by EBSD analysis. The value of the identified factor was 1.2 in this study.

### 2.3. Mechanical properties of the material

A uniaxial tensile test was performed at RT ( $\sim 20^\circ\text{C}$ ) under a strain rate of  $0.025\% \text{ s}^{-1}$  in accordance with DIN EN ISO 6892-1 until failure (Figure 4). The strain rate plays an important role in austenitic stainless steel since changes to the rate affect the mechanical behavior and microstructural evolution. Several

researchers have examined the effect of this parameter and have shown that by increasing the strain rate, the yield stress increases, while the ultimate tensile stress and the VFM decrease (Acharya et al., 2019; Das et al., 2008; Haušild et al., 2010; Hedström et al., 2009; Shen et al., 2012). At high strain rate, the material cannot completely dissipate the heat induced by deformation, so there is enough heat to inhibit transformation. In addition, this heat reduces the nucleation sites and eventually the volume fraction of  $\alpha'$ -martensite (Hecker et al., 1982; Talonen et al., 2005). In this study for quasi-static tests, the strain rate considered was low enough not to inhibit martensitic transformation.

The VFM was measured using the FERITSCOPE during the tensile test and as one can see in Figure 4, the amount of martensite formation monotonically increased with increasing strain. The VFM after failure of the specimen was about 0.9%. As high nickel content enhances austenite stability, the material studied, which contained 9.32% nickel underwent a limited amount of martensitic transformation at RT even at high deformation due to the stability of the austenite. Hence, the material studied was not metastable at RT (Christ et al., 2015).

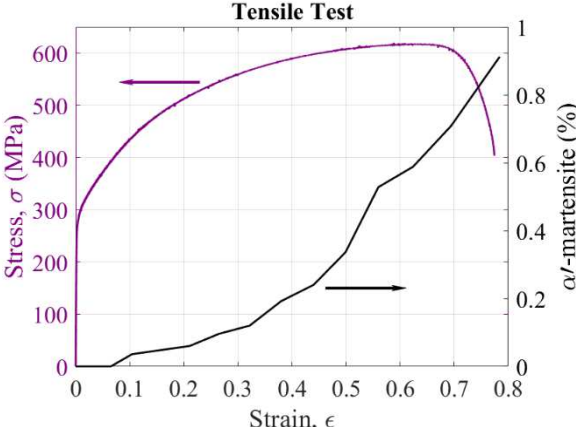


Fig. 4. Engineering stress-strain curve and VFM versus strain

The mechanical properties obtained from the 304L austenitic stainless steel are summarized in Table 2. The yield strength is determined by an offset of 0.2%. A uniform elongation with final value of 78% and tensile strength of 617 MPa at RT are indicators of the high ductility of this material.

Table 2. Mechanical properties of 304L austenitic stainless steel

Material	Young's modulus (GPa)	R 0.2% (MPa)	Tensile strength (MPa)	Elongation after fracture (%)
Stainless steel 304L	201	271	617	78

In addition to strain rate, testing temperature can also significantly affect the mechanical properties and the martensitic transformation of the austenitic stainless steel. By decreasing the test temperature, the

ultimate tensile strength, toughness and deformation-induced  $\alpha'$ -martensite increase while elongation at fracture decreases (De et al., 2006; Hahnenberger et al., 2012; Liu and Kaoumi, 2018; Müller-Bollenhagen et al., 2010b; Saint-Sulpice et al., 2014; Zheng and Yu, 2018). For more investigation, several uniaxial tensile tests until 30% strain were performed at different temperatures from -130°C up to 100°C. The effect of the testing temperature on the mechanical behavior of the material especially on the yield stress can be clearly seen in Figure 5 (a). This effect is amplified at temperatures of -90°C and -130°C, where a secondary hardening appears and the shape of the stress-strain curve changes to the sigmoidal form. As shown in Figure 5 (b), the yield stress at 0.2% decreased as the testing temperature increased, which is in good agreement with the findings of the literature (Byun et al., 2004; Desu et al., 2016; Zheng and Yu, 2018). Furthermore, after carrying out tensile tests at different temperatures, the volume fraction of  $\alpha'$ -martensite was measured using the FERITSCOPE at seven different points through the gauge length for each specimen and an almost uniform distribution of  $\alpha'$ -martensite was seen. These measurements will be discussed in detail in Section 4. Obviously, the volume fraction of  $\alpha'$ -martensite increased with a decrease in the test temperature. This increase in  $\alpha'$ -martensite was responsible for the hardening of the material (Talonen et al., 2004).

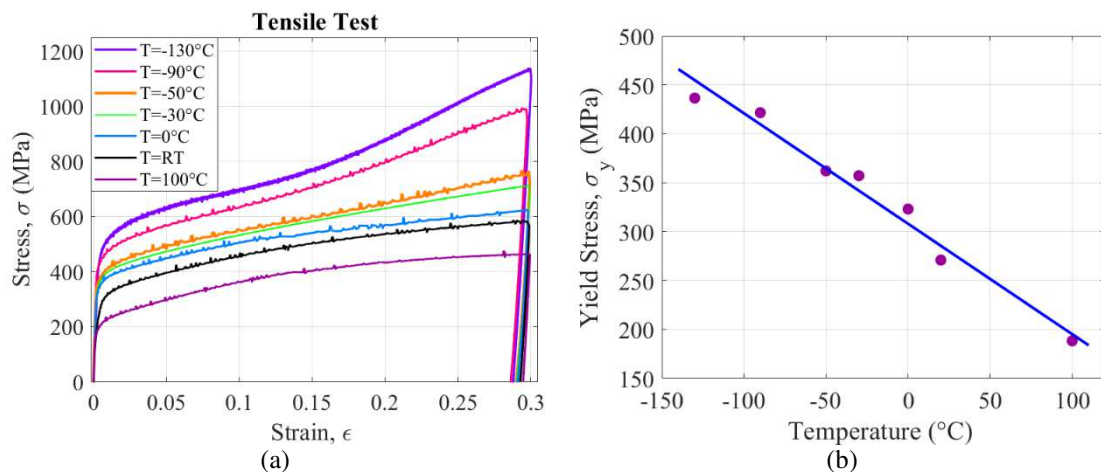


Fig. 5. (a) Uniaxial tensile tests at different temperatures until 30% strain (b) evolution of yield stress versus temperature

### 3. Self-heating assessment under different condition

#### 3.1. Self-heating test procedure

SH tests consist of a series of cyclic loading (or loading blocks) with increasing stress amplitude for the same specimen. At each stress amplitude, the cyclic loading is carried out with the same frequency and the number of cycles and the temperature elevation is recorded. There are two steps for each loading

block; the first is the loading step (between time  $t_0$  and  $t_1$  in Figure 6) where the specimen is subjected to the specified number of cycles under sinusoidal load control condition. The second is a cooling step (between time  $t_1$  and  $t_2$ ), during which the cyclic loading is interrupted in order to cool the specimen down to the initial temperature ( $T_0$ ). This protocol is repeated for each loading block, and the temperature evolution relevant to each stress amplitude is recorded. **When the temperature rise does not stabilize after achieving the desired number of cycles, the cyclic loading is stopped.**

As a zero-dimensional (0D) approach was adopted (which will be detailed in the following), the mean value of the temperature field over the gauge length can be considered as the specimen temperature ( $T_{specimen}$ ). Since the temperature field is assumed to be homogeneous in this approach, the temperature of the specimen center is measured by the thermocouple. On the other hand, the **temperature evolution in the jaws** during cyclic loading may produce extra heating in the specimen. Therefore, to obtain the real temperature evolution of the specimen corresponding to the intrinsic thermal dissipation, the mean temperature of the jaws ( $1/2 \times (T_{upper\ jaw} + T_{lower\ jaw})$ ) is subtracted from  $T_{specimen}$  and the mean temperature change ( $\theta^{0D}$ ), which is given by Equation (1), is registered during the test.

$$\theta^{0D} = T_{specimen} - (T_{upper\ jaw} + T_{lower\ jaw})/2 \quad (1)$$

The temperature rise reaches a stabilized value after a specific time (Figure 6). This stabilized mean steady state temperature ( $\bar{\theta}^{0D}$ ) is determined for each loading block and is plotted versus stress amplitude which is the so-called SH curve (Doudard et al., 2005; Munier et al., 2014).

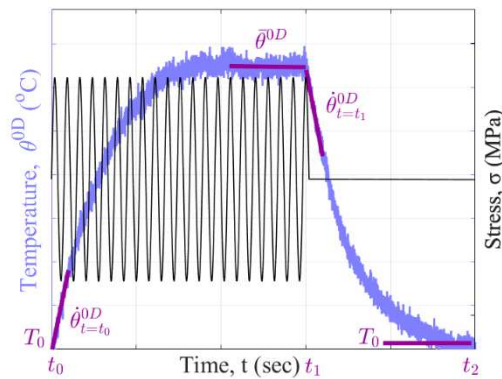


Fig. 6. Temperature and stress evolution versus time during one loading block

The temperature evolution during loading blocks with different stress amplitudes for the material studied is indicated in Figure 7; this SH test was performed at stress amplitudes of 50 up to 370 MPa (the stress amplitudes considered in this test are shown in Figure 8). All loading blocks were carried out with a

loading ratio  $R = -1$ , a testing frequency ( $f$ ) of 10 Hz and a number of cycles of 6000 per block. For the sake of clarity, only stress amplitudes between 140 and 370 MPa were plotted. This figure shows that the temperature increases rapidly at the beginning of the test (during the first 2000 cycles) and then it tends to reach a stationary value. This stabilization corresponds to a constant dissipated thermal source (i.e., a thermodynamic equilibrium between the heat loss with the surroundings and energy induced by mechanical loading). The higher stress amplitudes lead to the higher mean steady state temperature following the same trend until it reaches about  $35^{\circ}\text{C}$  for a stress amplitude of 350 MPa. At higher stress amplitudes, the temperature does not stabilize and it ramps up to  $43^{\circ}\text{C}$  after 6000 cycles. In contrast, for stress amplitudes between 50 MPa and 100 MPa, the evolution in temperature is negligible and for the values less than 140 MPa, it remains lower than  $0.8^{\circ}\text{C}$ . At the end of each loading step, the testing machine is stopped but temperature measurements continue for 400 seconds to record the cooling step (i.e., the temperature decrease in the specimen after having stopped the test).

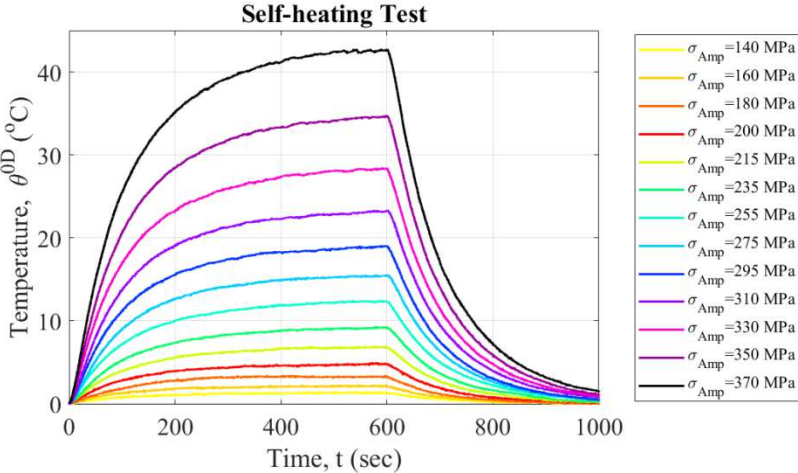


Fig. 7. Mean temperature evolution during different cyclic loading blocks

The SH curves on linear and logarithmic scale diagrams are shown in Figures 8a and 8b, respectively. In these curves, the two last loading blocks (i.e. stress amplitudes of 360 MPa and 370 MPa), where the temperature evolution does not stabilize, are not considered.

From the logarithmic scale diagram, different SH regimes and their slopes can be identified. The number of regimes is different for various materials. For metals, generally two regimes exist (Munier et al., 2014), while for some composites e.g. short fiber reinforced thermoplastics, three regimes (Abello et al., 2013) and for austenitic steel of X4CrNiMoN 21-9-4, only one regime (Puget, 2013) are observed. For the material studied at room temperature (on the specimen with or without PS) and at low temperatures,

one SH regime is always observed. The SH curve on the logarithmic scale plus or minus the precision error ( $\bar{\theta}^{OD} \pm \Delta\theta$ ) of the thermal measurements with the thermocouple ( $\Delta\theta = 0.1 \text{ }^\circ\text{C}$ ) is plotted in Figure 8b (i.e., green curves). Since the slopes of the regimes are an indicator for the SH phenomenon (Munier et al., 2014), their calculation is important. As it is clear in this figure, there is only one SH regime with a slope value of  $3.6 \text{ }^\circ\text{C}/\text{MPa}$ .

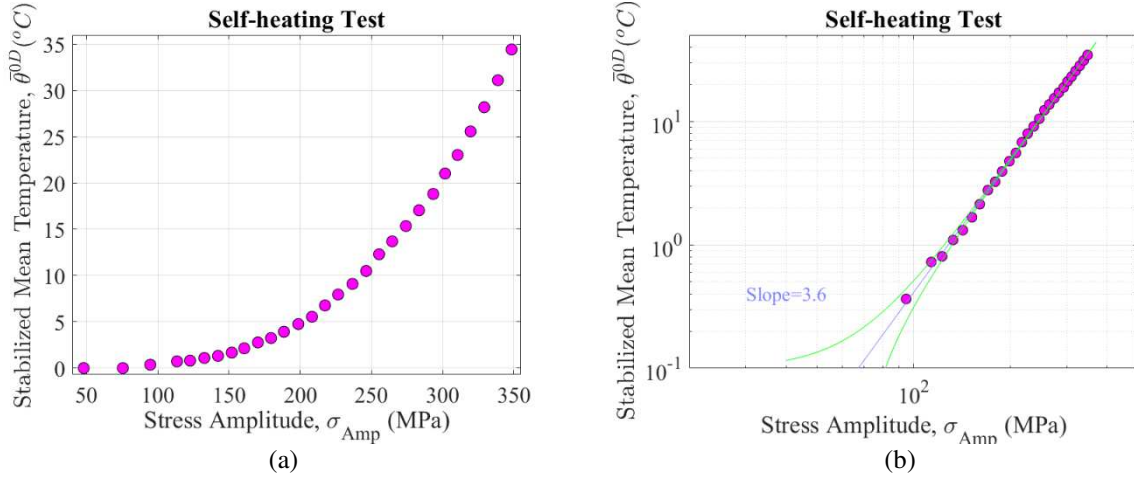


Fig. 8. SH curve on (a) linear (b) logarithmic scale diagrams

After describing the testing process, in the following, more details about the OD approach and different post-processing methods of the SH tests are discussed.

The energy dissipated from the material subjected to cyclic loadings generates a thermal field, the extent of which depends on different parameters such as the volume and the sample geometry, the material thermal properties, the thermal boundary conditions and the intensity of the thermal source due to the irreversible mechanisms. This generated heat leads to the material SH. In fact, the SH phenomenon is a representation of the energy dissipated in the material. The heat equation enables the relationship between the amount of dissipated energy and the corresponding SH magnitude to be established. The local form of the heat equation, which is derived from the principle of energy conservation, can be written as:

$$\rho c \dot{T} + \text{div}(\vec{q}) = \Delta + r + \rho T \frac{\partial^2 \psi}{\partial \varepsilon^e \partial T} : \dot{\varepsilon}^e + \rho T \frac{\partial^2 \psi}{\partial V_k \partial T} : \dot{V}_k = \rho c S_t \quad (2)$$

The left-hand side of Equation (2) defines the heat absorption ( $\rho c \dot{T}$ ) and the heat losses by conduction ( $\text{div}(\vec{q})$ ). Where  $T$ ,  $c$ ,  $\rho$  and  $\vec{q}$  are the temperature, the heat capacity, the density and the heat flux vector, respectively. The right-hand side of Equation (2) describes the local thermal source  $S_t$ , which consists of

the intrinsic dissipated energy ( $\Delta = \sigma : \dot{\varepsilon}^p - A_k : \dot{V}_k$ ), the external heat supply ( $r$ ) and the thermodynamic coupling source ( $\rho T \frac{\partial^2 \psi}{\partial \varepsilon^e \partial T} : \dot{\varepsilon}^e + \rho T \frac{\partial^2 \psi}{\partial V_k \partial T} : \dot{V}_k$ ). Where  $\sigma$  is the stress tensor,  $\varepsilon^e$  is the elastic strain tensor,  $\varepsilon^p$  is the plastic strain tensor,  $A_k$  denotes a set of thermodynamic forces associated to a set of the internal variables  $V_k$  and  $\psi$  is the Helmholtz free energy.

Since the temperature variations upon cyclic loadings can be considered to be small, one can assume that:  $c$  is independent of the temperature, the external heat supply is time-independent, the thermomechanical coupling source is negligible (i.e.,  $\rho T \frac{\partial^2 \psi}{\partial V_k \partial T} : \dot{V}_k \sim 0$ ) and the convective terms of the material time derivative are negligible (i.e.,  $dT/dt = \partial T/\partial t$ ). On the other hand, by supposing a homogenous temperature field throughout the volume of the specimen, the 0D approach can be considered (i.e. the thermal source is spatially homogeneous in the volume considered). By integrating Equation 2 over the volume and by considering the above-mentioned assumptions, one can obtain the following expression (Doudard et al., 2010, 2005):

$$\dot{\theta}^{0D}(t) + \theta^{0D}(t)/\tau_{eq}^{0D} = S_t^{0D}(t) \quad (3)$$

where  $\theta^{0D}$  is the elevation of the mean temperature in the volume,  $\tau_{eq}^{0D}$  is a characteristic time representing heat losses with the surroundings and  $S_t^{0D}$  is the mean value of the thermal source throughout the material volume, which can be broken down into an intrinsic dissipation and a thermoelastic coupling term (i.e.,  $\rho T \frac{\partial^2 \psi}{\partial \varepsilon^e \partial T} : \dot{\varepsilon}^e$ ). By integrating the heat sources ( $S_t^{0D}$ ) over one cycle, the sum of thermoelastic coupling effects becomes null and the value of the average thermal source per cycle ( $\bar{S}_t^{0D}$ ) is given by:

$$\dot{\theta}_{cycle}^{0D}(t) + \theta_{cycle}^{0D}(t)/\tau_{eq}^{0D} = \bar{S}_t^{0D} = f_r \int_{cycle} S_t^{0D} dt = f_r / \rho c \int_{cycle} \Delta dt = f_r D / \rho c \quad (4)$$

where  $f_r$  is the loading frequency and  $\theta_{cycle}^{0D}$  is the mean value of temperature evolution per cycle.

If the average value of heat source per cycle ( $\bar{S}_t^{0D}$ ) is constant, three different cases can be considered:

Case I. At the early beginning of each loading block ( $t = t_0 = 0$ ), the temperature evolution is negligible, i.e.,  $\theta_{cycle}^{0D} \sim 0$  and based on Equation 4,  $\dot{\theta}_{cycle}^{0D}(t = t_0) = \bar{S}_t^{0D}$ .

Case II. At the end of loading step of each loading block (where the temperature reaches a stabilized mean value,  $\bar{\theta}_{cycle}^{0D}$ ), the temperature rate is negligible, i.e.,  $\dot{\theta}_{cycle}^{0D} \sim 0$  and based on Equation 4,  $\bar{\theta}_{cycle}^{0D} = \tau_{eq}^{0D} \times \bar{S}_t^{0D}$ .

Case III. At the beginning of the cooling step (where the loading is stopped in order to thoroughly cool down the specimen), the heat sources have vanished, i.e.,  $\bar{S}_t^{0D} = 0$  and based on Equation 4,  $\dot{\theta}_{cycle}^{0D}(t = t_1) = -\bar{\theta}_{cycle}^{0D}/\tau_{eq}^{0D}$ .

It is expected that the SH curves obtained by these three methods lead to similar results. To investigate this claim, the SH curves of the previously mentioned test, are obtained by these three methods and the results are compared. In the first case, the SH curve can be extracted by fitting a line at  $t = t_0$  through the temperature-time curve for each loading block. The slope of the fitted line ( $\dot{\theta}^{0D}(t_0)$  obtained for the time range between 10 and 50 seconds in Figure 6) corresponds to the intrinsic dissipation. This temperature rate ( $\dot{\theta}^{0D}(t_0)$ ) is determined for each loading block and it is plotted versus stress amplitude (green curve in Figure 10). This method has mostly been used for composite (Abello et al., 2013) and elastomer (Masquelier et al., 2015) materials.

The stabilized average temperature rise, denoted by  $\bar{\theta}^{0D}$ , is considered for plotting the SH curve in the second case. This  $\bar{\theta}^{0D}$  is gained by averaging the temperature when it stabilizes (Figure 6). In this case, the intrinsic dissipation is calculated by dividing the stabilized mean temperature over the characteristic time. The characteristic time in the 0D approach depends on the dimensions of the specimen, the thermal conductivity of the material and the exchange coefficients between the jaws and the specimen and between the specimen and the environment. The least squares method is used to identify the characteristic time by fitting the experimental results on Equation 5 on the  $t_1$  to  $t_2$  part of the curve (Figure 6), where the temperature returns to its initial thermal state ( $T_0$ ). The characteristic time can be also obtained using the loading step (i.e., at the time between  $t_0$  and  $t_1$ ). In the loading step, the characteristic time depends on the loading frequency, hence, in this study, the second part (i.e., the cooling step) is used to obtain this characteristic time. Equation 5 is a solution of Equation 4, when  $\bar{S}_t^{0D} = 0$  (i.e., during the cooling step). The results of this identification are presented for six loading

levels (for the sake of clarity) in Figure 9. It would appear that the characteristic times obtained are constant.

$$\theta_{cycle}^{0D} = \bar{\theta}_{cycle}^{0D} \times \exp(-t/\tau_{eq}^{0D}) \quad (5)$$

The intrinsic dissipation is obtained by dividing the corresponding  $\bar{\theta}^{0D}$  over the identified characteristic time and the results are plotted in Figure 10 (the blue curve).

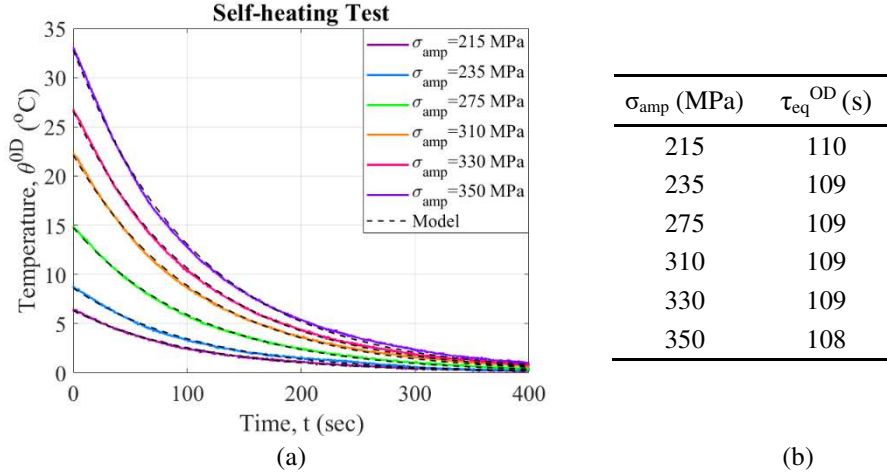
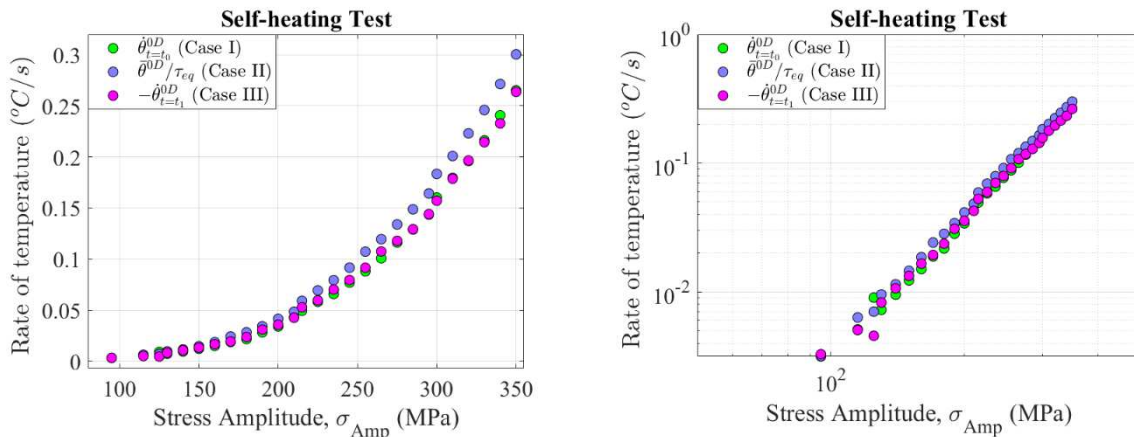


Fig. 9. (a) Identification of characteristic time ( $\tau_{eq}^{0D}$ ) using the cooling part of the temperature-time curves (b) table of the values obtained from curve fitting

In the third case, the SH curve can be plotted by fitting a line at  $t = t_1$  through the temperature-time curve ( $\dot{\theta}^{0D}(t_1)$  in Figure 6). This temperature rate ( $\dot{\theta}^{0D}(t_1)$ ) is determined for each loading block and is plotted versus the corresponding stress amplitude (pink curve in Figure 10). Since, the slope of the fitted line is negative in this case, its absolute value is considered in order to compare the results with those obtained in cases I and II.

Figure 10 indicates that the SH curves obtained by these three methods are in good agreement. Consequently, in the rest of this study, the second method (the common one) will be used to plot the SH curves.



(a) (b)  
Fig. 10. Comparison of SH curves obtained from three different methods on (a) linear (b) logarithmic scale diagrams

After obtaining the SH curve, an empirical approach can be used to estimate the fatigue limit as shown in the literature (Doudard et al., 2005; Munier et al., 2014). In this method, the intersection of the asymptote at the two or three last points of the SH curve with the x-axis gives a good empirical estimation of the mean value of fatigue limit. The capability of this approach to predict the fatigue limit has been verified on a wide range of metals, by performing the classic fatigue tests, as mentioned in the introduction. In the case of austenitic stainless steel, this approach can be used as a fast and applicable method, but its results have yet to be verified. Confirming the fatigue limit obtained by this method with those gained using classic fatigue tests is out of the scope of this paper. In the following, this approach will be applied for a quantitative comparison of the fatigue limit values obtained under different conditions.

### 3.2. Influence of the loading frequency

As the loading frequency is an important parameter for the SH of the specimen, it is necessary to check its effect before studying the effect of other parameters. To this end, three different frequencies of 3 Hz, 10 Hz and 20 Hz are considered. The SH curves obtained on the linear and logarithmic scale diagrams are shown in Figures 11a and 11b, respectively. Based on Equation 4, the loading frequency is a parameter that can modify the thermal source. Therefore, increasing the loading frequency amplifies the stabilized mean temperature of the material. Hence, in this section, the stabilized mean temperature is normalized by dividing the temperature rise over the loading frequency. It can be noted that the SH curves obtained for all frequencies are in good agreement. Thus, the evolution of stabilized mean temperature can be considered as a linear function of the frequency, similar to other metals (Munier et al., 2014). It means that the **intrinsic** dissipation source of SH in the material studied is nearly constant.

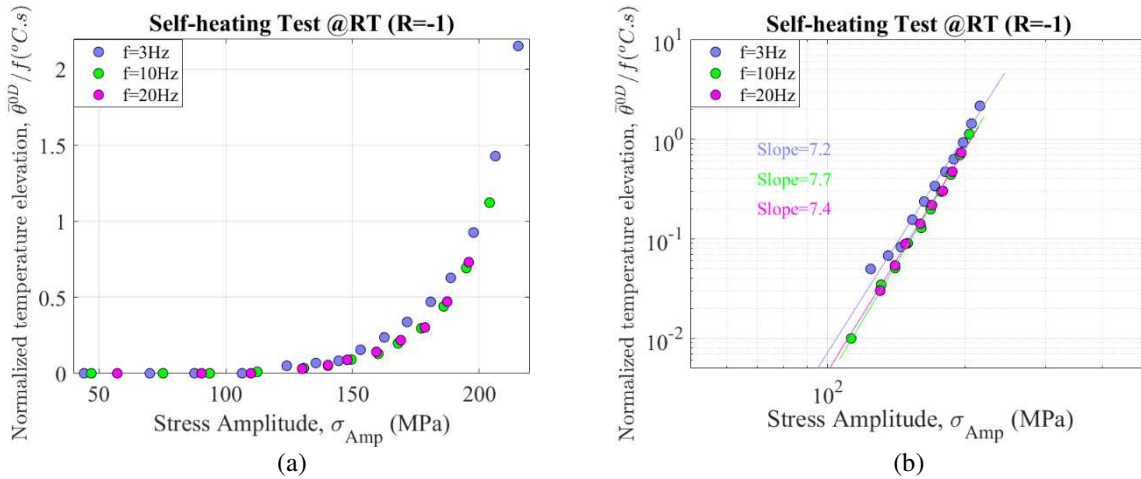


Fig. 11. SH curves obtained with different loading frequencies on (a) linear (b) logarithmic scale diagrams

Since, the frequency does not have a notable effect on the SH results, in the following, the frequency of 10Hz and the number of cycles equal to 6000 are considered for each loading block. In addition, all tests were carried out under load control and  $R=-1$ .

### 3.3. Influence of the testing temperature

One of the important parameters for investigating the SH behavior of the austenitic stainless steel could be the temperature at which the tests have been performed. Figures 12a and 12b show the results of SH tests at three different temperatures such as RT ( $\sim 20^{\circ}\text{C}$ ),  $0^{\circ}\text{C}$  and  $-30^{\circ}\text{C}$  on linear and logarithmic scale diagrams, respectively. [The environment temperature was controlled by a thermal chamber during these tests and the temperature inside the chamber was kept constant.](#) By decreasing the test temperature from RT to  $-30^{\circ}\text{C}$ , the mechanical properties of the material seem to be improved as mentioned before. For instance, the yield stress of the material increased from 270 MPa to 357 MPa. Therefore, the specimen needs a higher stress amplitude value to achieve the same amount of [intrinsic](#) dissipation (e.g. for the stabilized mean temperature of  $4.4^{\circ}\text{C}$  (Figure 12a), the stress amplitudes of 185 MPa, 205 MPa and 220 MPa are required at testing temperatures of  $20^{\circ}\text{C}$ ,  $0^{\circ}\text{C}$  and  $-30^{\circ}\text{C}$ , respectively). Hence, the SH curves shifted to the right, which could mean that the fatigue limit of the material is improved by decreasing the testing temperature.

After the SH test, the VFM was measured using the FERITSCOPE and the maximum value of  $\alpha'$ -martensite for these tests was lower than 0.5%. Since, in the SH test procedure, the stress must stay lower than the yield strength, there was not enough mechanical driving force to start the martensitic transformation (Krupp et al., 2008; Talonen, 2007). In addition, the SFE of the material studied was

higher than 18 mJ/m<sup>2</sup> and as previously mentioned, in this case, the direct transformation happened through strain-induced transformation and not stress-induced transformation (Shen et al., 2012). Therefore, this low amount of martensite was predictable. As a conclusion from the results obtained, one can say that the martensitic transformation does not have a notable influence on the SH results and the improvement of the fatigue limit could be due to the temperature effect on the mechanical properties of the material.

The results in Figure 12b demonstrate that there is only one SH regime with identified slopes of 7.7 °C/MPa, 6.9 °C/MPa and 8 °C/MPa for the test temperatures of 20°C, 0°C and -30°C, respectively. The slope of each curve is shown using the same color as the corresponding curve.

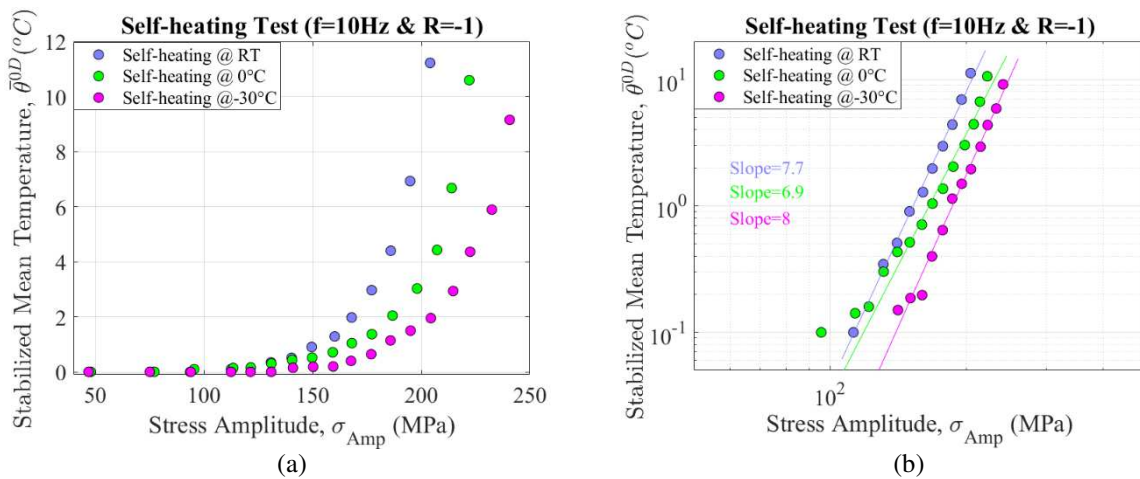


Fig. 12. SH curves at different temperatures on (a) linear (b) logarithmic scale diagrams

### 3.4. Influence of pre-strain at room temperature

In this section, the effect of PS at RT is investigated through SH tests. In order to study this effect, three different states of the material namely without PS (0% PS), with 15% PS and 30% PS were selected. As clearly shown in Figure 13a, the increase in the PS values at RT result in a shift of the SH curves to the right. This could imply improvement in the fatigue life. These results are in accordance with those presented by (Gupta et al., 2018). [These authors stated that every 20% increment in pre-straining caused a 40 to 80 MPa enhancement in the fatigue life.](#)

After these SH tests, the volume fractions of  $\alpha'$ -martensite were measured using a FERITSCOPE and no quantifiable transformation was found even after performing an SH test on the 30% pre-strained specimen. These results are in line with the findings of (De et al., 2006), stating that the deformation at

RT does not initiate any measurable transformation up to 30% strain. Therefore, it should be noted that these curves show the influence of the plastic strain and not the effect of the martensitic transformation.

Figure 13b depicts the SH curves at three PS levels on the logarithmic scale. One SH regime with different slopes is illustrated for these three PS levels. The slope of the SH curve without PS is 7.7 °C/MPa, while for the pre-strained samples (i.e., 15% PS and 30% PS) it is 4 °C/MPa and 3.7 °C/MPa, respectively.

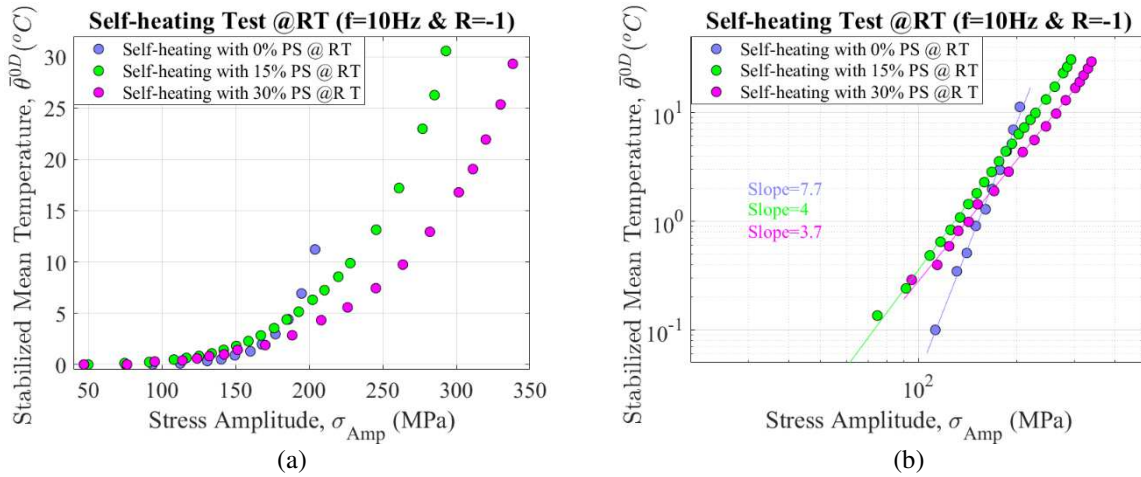


Fig. 13. SH curves after different PS levels on (a) linear (b) logarithmic scale diagrams

### 3.5. Influence of a complex thermomechanical history

As previously stated, no martensitic transformation occurred during the SH tests performed on the virgin specimens at different temperatures and on the pre-strained specimens at RT. Therefore, to study the effect of martensite fraction on the SH behavior, two different material initial states were considered: One state along with martensitic transformation (case 1 in Figure 14 (a)) and another without martensitic transformation (case 2 in Figure 14 (a)). On the one hand, for temperatures higher than  $M_s$  (the martensite start temperature) with sufficient mechanical driving force that is supplied by applying stress or strain, martensitic transformation can occur (Christ et al., 2015; Krupp et al., 2008). Therefore, several tensile tests up to 30% strain were performed at a wide range of temperatures between -130°C to RT (case 1 in Figure 14 (b)). Hence, there was a material state with the same inelastic strain but different VFM (due to different PS temperatures). Then, the SH tests at RT were conducted on these pre-strained specimens (case 1 in Figure 14 (c)). On the other hand, for temperatures higher than  $M_d$  (i.e., the maximum temperature at which martensitic transformation can be induced by plastic deformation), there was no phase transformation due to high SFE and a low chemical driving force (Hedström et al., 2009;

Olson and Cohen, 1972; Sugimoto, 2009) and hardening was only due to plastic strain. Thus, after applying 30% PS at 100°C (case 2 in Figure 14 (b)) and subsequently performing an SH test at RT on this pre-strained specimen (case 2 in Figure 14 (c)), the VFM was almost zero. Therefore, by using this method and comparing the results obtained from these two cases, the effect of the martensite fraction can be studied on the SH curves.

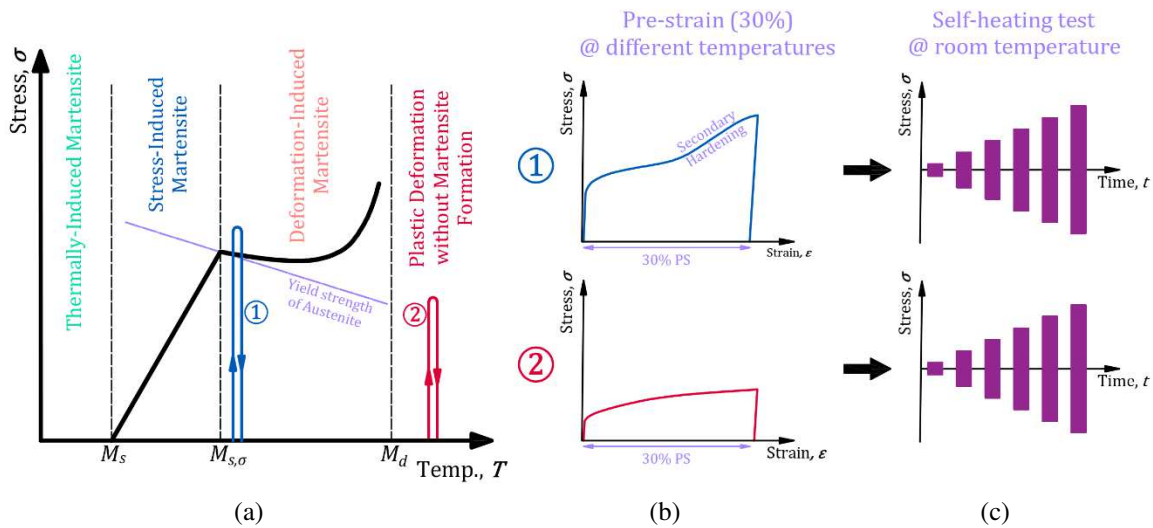


Fig. 14. Schematic illustration of (a) pseudo-diagram of metastable materials with the loading paths considered (b) conducting PS at different temperatures (c) performing the SH tests at RT on the pre-strained specimens

The SH curves at RT obtained on pre-strained specimens are demonstrated in Figure 15(a). As one can see in this Figure, by decreasing the test temperature, there are two different trends. From 100°C up to -50°C, the SH curves shifted to the left, and with a further decrease from -90°C to -130°C, an inverse trend can be seen. Since, for the material with the same inelastic strain, lower temperatures lead to higher VFM and given that, the martensite phase has a higher strength than the austenite, a secondary hardening in tensile curves can appear, which is schematically shown in case 1 in Figure 14 (b). This secondary hardening causes an improvement in the mechanical properties and the fatigue limit of the material (Gupta et al., 2018; Müller-Bollenhagen et al., 2010a; Shen et al., 2012; Talonen et al., 2004). Therefore, the secondary hardening relevant to pre-straining at temperatures of -90°C and -130°C (Figure 5(a)) can be a reason for the shift of the corresponding SH curves to the right. On the other hand, in these curves, the effect of plastic strain and martensite fraction simultaneously exists and it is complex to explain their effects separately. Consequently, microstructural observations and further investigations are required to justify the origin of this particular trend and will be presented in the following sections. It is worth noting

that only one SH regime with a slope of about 3 °C/MPa is observed for these pre-strained specimens on a logarithmic scale (Figure 15(b)).

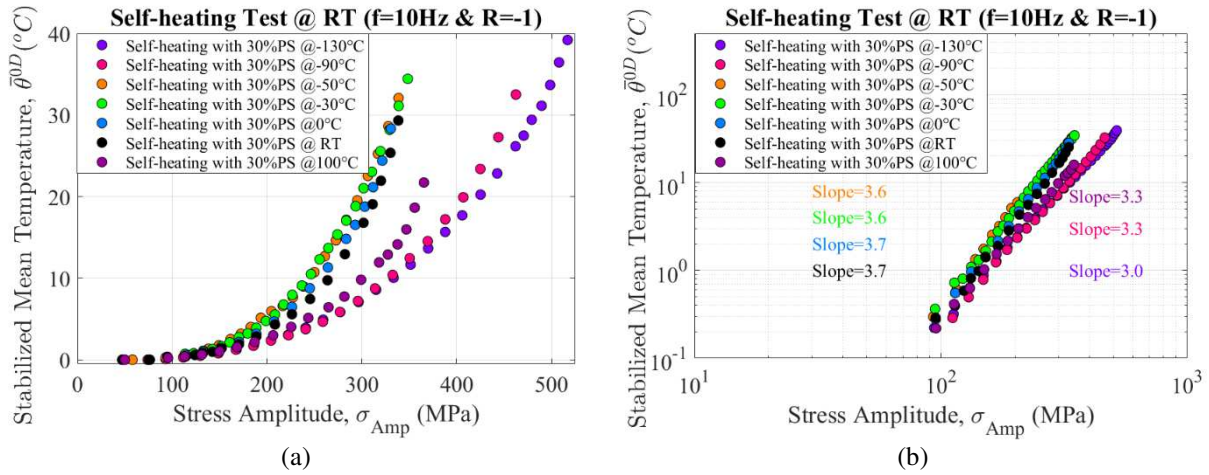


Fig. 15. SH curves with different volume fractions of martensite on (a) linear (b) logarithmic scale diagrams

Since, applying 30% PS at different temperatures leads to changes in the yield stress of the material at RT, to identify this yield stress evolution, one can apply additional 10% PS at RT to the pre-hardened specimens up to 30% at different temperatures. In Figure 16 (a), the stress-strain curves obtained during 30% PS at different temperatures together with the stress-strain curves obtained by subsequently performing 10% PS at RT are shown. In this figure, the yield stress at RT after cold pre-straining is lower than that at low temperatures. For instance, the RT yield stress for the specimen pre-strained at -130°C is 906 MPa, which is lower than the corresponding stress value at -130°C (1111 MPa at the end of loading step). These evolutions could be due to the effect of temperature on the yield stress. In contrast, the yield stress at RT after hot pre-straining is higher than that at high temperature (i.e., 100°C). The evolution of the yield stress at RT after pre-straining at different temperatures is depicted in Figure 16 (b). As one can see in this figure, the yield stress at RT decreases by increasing the pre-straining temperature.

Moreover, the slopes of stress-strain curves during the 10% PS at RT (shown in Figure 16 (a)) are approximately constant, while the corresponding slopes during 30% pre-straining at lower temperatures progressively increase, especially at higher strain values (i.e., strain values between 20% and 30%). This increase in the slope of the stress-strain curves at lower temperatures is due to martensitic transformation, which caused secondary hardening (e.g., at temperatures of -90°C and -130°C). Thus, one can state that the constant slope of stress-strain curves at RT is more due to plasticity. Hence, by eliminating the evolution of the yield stress, one can investigate the effect of the martensite fraction on the SH curves.

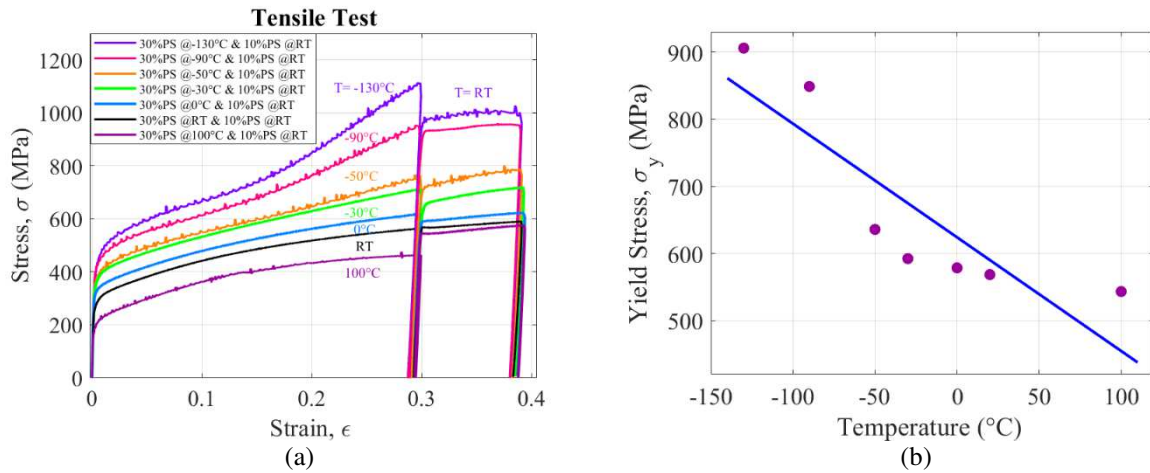


Fig. 16. (a) Uniaxial tensile tests until 30% strain at different temperatures and subsequently 10% strain at RT (b) evolution in the yield stress at RT after pre-straining at different temperatures

In order to decouple the effect of the martensite fraction on the SH behavior from its effect on the yield stress, the stress amplitudes were normalized by the yield stress values identified at RT after pre-straining at different temperatures. Figure 17(a) shows the SH curves after this normalization. As one can observe in this figure, by decreasing the pre-straining temperatures from 100 $^{\circ}\text{C}$  to -130 $^{\circ}\text{C}$ , all SH curves shifted to the left and thus, the material could endure more heat; i.e., at the same normalized stress amplitude, the specimens containing more VFM experienced higher stabilized mean temperatures. A closer look at this figure illustrates that after normalization, the SH curves on the pre-strained specimen at temperatures of -50, -90 and -130 $^{\circ}\text{C}$  are almost the same. Therefore, one can state that for pre-strained specimens at temperatures lower than -50 $^{\circ}\text{C}$ , the effect of the martensite fraction on the normalized SH curves was almost identical. In addition, in the logarithmic scale (Figure 17(b)), only one SH regime with a slope of about 3 can be seen for all the SH curves.

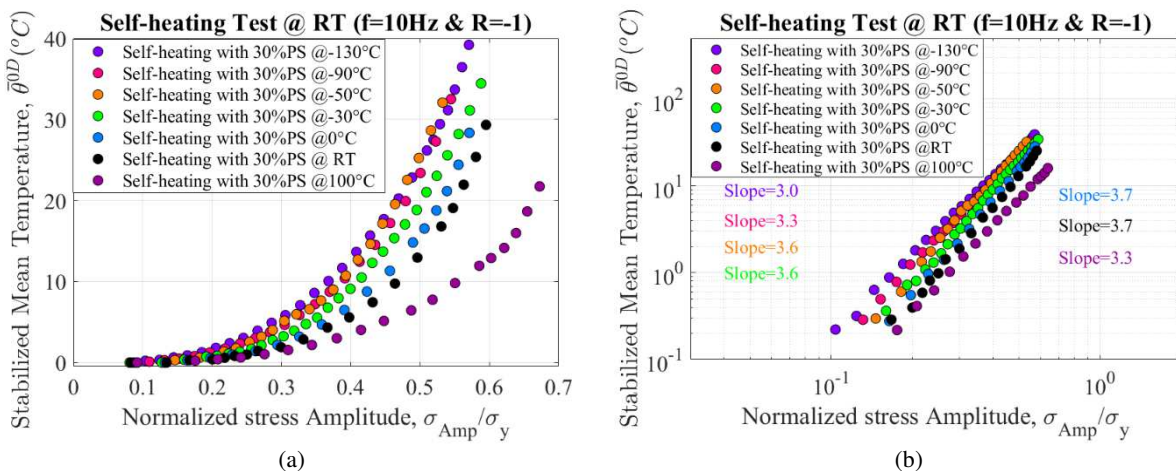


Fig. 17. SH curves after normalization of stress amplitude on (a) linear (b) logarithmic scale diagrams

#### 4. Microstructure evolution analysis

The VFM after applying PS at different temperatures was measured using a FERITSCOPE at seven different points with a distance of 5mm from each other through the gauge length (which is shown schematically in Figure 18) and an almost uniform distribution of martensite is seen. In Figure 18, dash lines demonstrate the VFM measured after 30% PS at different temperatures. In addition, after each SH test at RT, the VFM was measured once again and no significant change was seen (solid lines in Figure 18). One can note that the VFM increases by decreasing the test temperature.

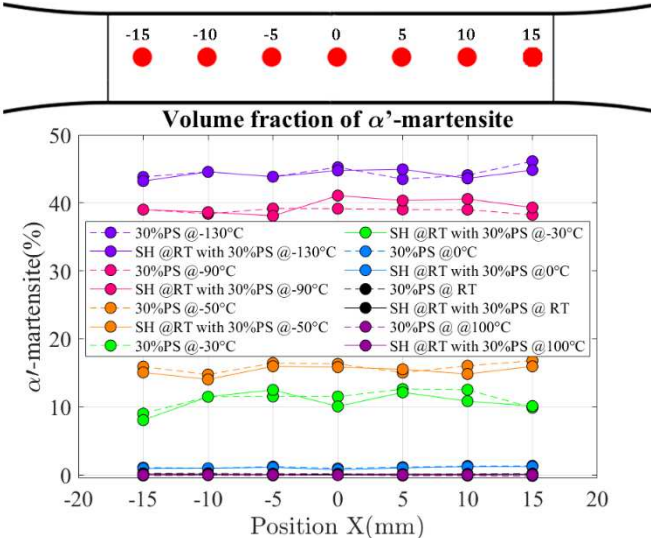


Fig. 18. Volume fraction of  $\alpha'$ -martensite measured using FERITSCOPE after 30%PS at different temperatures and after SH tests at RT on pre-strained specimens

To confirm the volume fraction of  $\alpha'$ -martensite obtained using the FERITSCOPE, EBSD analysis was used. The band contrast maps after SH tests at RT on pre-strained specimens are indicated in Figures 19(a) to 19(f) to characterize the morphological features on the microstructures and to investigate the microstructural changes related to PS at low temperatures. At PS temperatures of RT and 0°C, some shear bands appear in a few austenitic grains. These initial shear bands are parallel to each other and nucleate more at grain boundaries. By decreasing the temperature, they grow more into the austenite grain. At temperatures less than -30°C, the nucleated shear bands intersect each other, which is due to the activation of the secondary slip systems (Hedström et al., 2009) and some dark areas arise, which can be considered as martensite. These dark areas are more visible in the junction of shear bands with grain boundaries or twins at temperatures of -30°C and -50°C, while at lower temperatures, they cover most of the austenite grains.

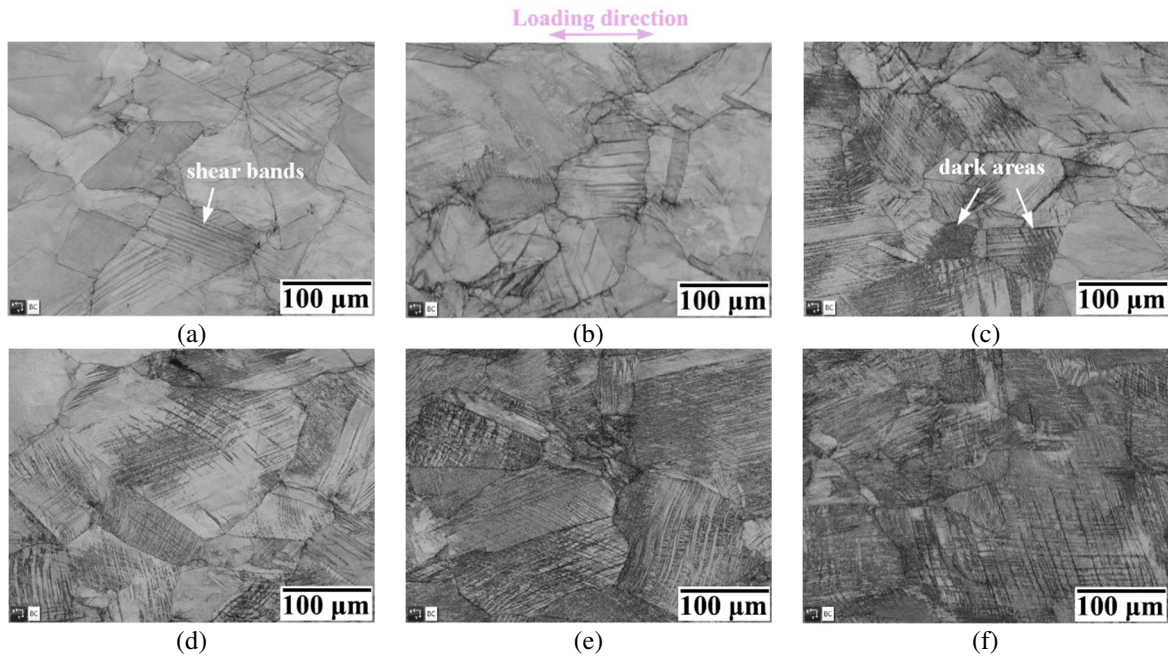


Fig. 19. Band contrast maps after SH tests at RT on the pre-strained specimens at temperatures of (a) RT (b) 0°C (c) -30°C (d) -50°C (e) -90°C (f) -130°C

To prove our supposition that the dark areas are a martensite, phase maps are used. These maps display the distribution of the different phases in the microstructure. Figures 20(a) to (f) show the phase maps of pre-strained specimens after SH tests at RT.  $\alpha'$ -martensite,  $\epsilon$ -martensite and austenite phases are represented by red, yellow and blue colors, respectively. To obtain the actual value of the volume fraction of phases, the selected area was sufficiently large. Mean Angular Deviation (MAD) was less than  $1^\circ$ , which shows a good match between the Kikuchi bands detected and the simulation. The “zero solutions” points that originate from non-indexing pixels were lower than 3%. As one can see in these figures, at temperatures of RT and 0°C, there is no significant amount of  $\alpha'$ -martensite, while at temperatures of -30°C and -50°C, the amount of  $\alpha'$ -martensite increases, as observed in some grains. By decreasing the temperature to -90°C and -130°C,  $\alpha'$ -martensite increasingly covers the grains as previously observed by (Hedström et al., 2009) who stated that for VFM higher than 25%, a continuous network of martensite is created. It can be observed that  $\alpha'$ -martensite forms at the inner of twins and close to the grain boundaries and the martensite which forms is in the shape of needles. The measured volume fraction of  $\alpha'$ -martensite was 0.06%, 0.15%, 11.36%, 14.12%, 40.16% and 46.01% at temperatures of RT, 0°C, -30°C, -50°C, -90°C and -130°C, respectively. One can state that for the same level of inelastic strain, the strain-induced martensite formation increases by decreasing the test temperature. It means that the amount of  $\alpha'$ -martensite is a function of temperature and PS. The VFM at

a temperature of 100°C, which is quantified by EBSD and FERITSCOPE, is around 0%. Therefore, the  $M_d$  temperature of the material studied is between RT and 100°C.

The amount of  $\epsilon$ -martensite determined for all the cases is less than 0.6%. As previously mentioned, for SFE higher than 18 mJ/m<sup>2</sup>, direct transformation occurs; since the SFE of the material studied is about 26 mJ/m<sup>2</sup>, therefore, direct transformation is expected and in this case there is no intermediate phase (i.e.,  $\epsilon$ -martensite). That is the reason for the low values of  $\epsilon$ -martensite that were observed in this study.

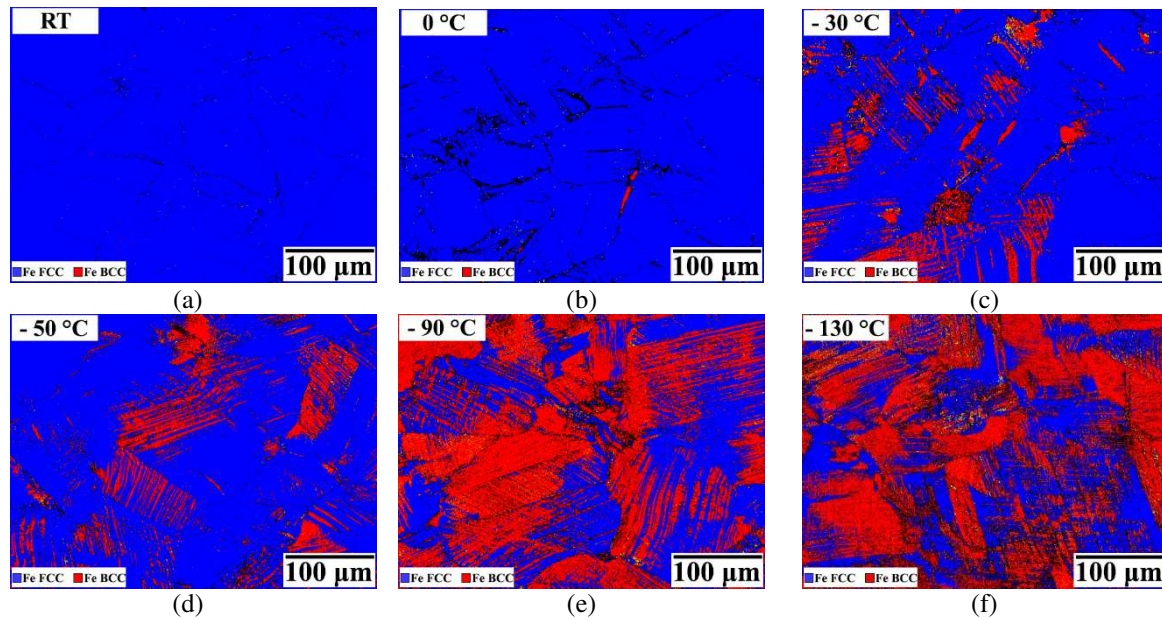


Fig. 20. Volume fraction of phases after SH tests at RT on the pre-strained specimens at temperatures of (a) RT (b) 0°C (c) -30°C (d) -50°C (e) -90°C (f) -130°C

The VFM measured by the FERITSCOPE shows good agreement with those obtained by EBSD (Figure 21). Based on the VFM measured in this section, one can state that for the amount of  $\alpha'$ -martensite between 0.09% and 15%, the behavior of the material in terms of SH response is similar (Figure 15) and represent a decrease in the fatigue life. On the contrary, for  $\alpha'$ -martensite values higher than 15% (i.e., 40% and 45%), an inverse behavior can be seen that could demonstrate an increase in the fatigue life. This increase in the fatigue limit may be due to the TRIP effect, which can strengthen the material and cause the appearance of a secondary hardening. Therefore, the optimal value of VFM for the material studied is higher than 15%. Classic fatigue tests with varying values of VFM will be performed to verify the determined optimal value of VFM in the continuation of the present work.

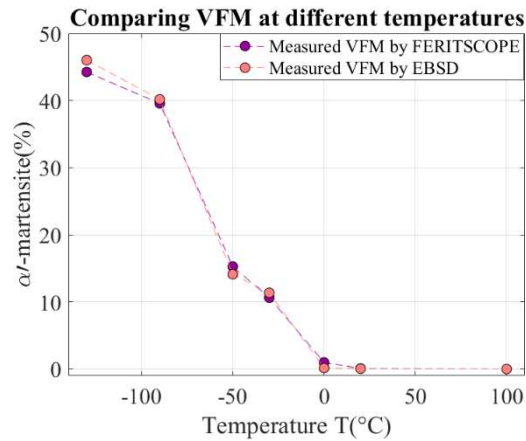


Fig. 21. Comparison of the VFM measured by FERITSCOPE and EBSD after SH tests at RT on the pre-strained specimens

## 5. Conclusion

The aim of this work was to study the effect of different parameters such as the testing temperature, the PS at RT and the initial VFM on the SH behavior of 304L austenitic stainless steel. The following conclusions have been drawn:

- (a) The mechanical properties and VFM changes during uniaxial tensile tests were evaluated. It was shown that decreasing the testing temperature increased the yield stress and the volume fraction of  $\alpha'$ -martensite.
- (b) Supposing a constant thermal source during cyclic loading, three methods can be considered to assess the SH response of the material. The results obtained from these three methods were almost in good agreement, which proved that the initial assumption was correct. Moreover, the procedure to obtain the characteristic time, which represents heat loss to the surroundings, was fully described.
- (c) Investigating the effect of the test temperature indicated that the SH curves shifted to the right with a decrease in the testing temperature. This could mean that the fatigue properties were improved by decreasing the testing temperature.
- (d) Increasing the PS values at RT resulted in the SH curves shifting to the right. This could imply an improvement in the fatigue properties.
- (e) Decreasing the temperature to within a band of 100°C to -50°C moved the SH curves to the left, whilst decreasing the temperature to within a band of -90°C to -130°C moved the curves to the right. Consequently, one can say that the optimum values (in respect of fatigue life improvement) of VFM for the material studied were higher than 15%. By normalizing the stress amplitude over the RT yield stress, the effect of the initial VFM on the SH behavior was decoupled from its effect on the yield stress. The

results have led us to conclude that for PS temperatures lower than  $-50^{\circ}\text{C}$ , the effect of martensitic transformation on the SH curves was identical. In other words, for VFM between about 15% and 45%, the SH behavior of material was the same.

(f) The VFM measured after all the SH tests showed that there is no phase transformation due to cyclic loading below the macroscopic yield stress.

This study represents a crucial first step toward the fatigue study of stainless steel materials using the SH method. Future work will concentrate on performing classic fatigue tests to confirm the conclusions made by conducting the SH tests.

### **Acknowledgments**

We kindly acknowledge the Region Bretagne, France, for partly financing the PhD scholarship of Behnaz Amini.

### **References**

- Abello, L.S., Marco, Y., Le Saux, V., Robert, G., Charrier, P., 2013. Fast Prediction of the Fatigue Behavior of Short Fiber Reinforced Thermoplastics from Heat Build-up Measurements. *Procedia Engineering* 66, 737–745. <https://doi.org/10.1016/j.proeng.2013.12.127>
- Acharya, S., Moitra, A., Bysakh, S., Nanibabu, M., Krishanan, S.A., Mukhopadhyay, C.K., Rajkumar, K.V., Sasikala, G., Mukhopadhyay, A., Mondal, D.K., Ghosh, K.S., Jha, B.B., Muraleedharan, K., 2019. Effect of high strain rate deformation on the properties of SS304L and SS316LN alloys. *Mechanics of Materials* 136, 103073. <https://doi.org/10.1016/j.mechmat.2019.103073>
- Allain, S., Chateau, J.-P., Bouaziz, O., Migot, S., Guelton, N., 2004. Correlations between the calculated stacking fault energy and the plasticity mechanisms in Fe–Mn–C alloys. *Materials Science and Engineering: A* 387–389, 158–162. <https://doi.org/10.1016/j.msea.2004.01.059>
- Bortoluci Ormastroni, L.M., Mataveli Suave, L., Cervellon, A., Villechaise, P., Cormier, J., 2020. LCF, HCF and VHCF life sensitivity to solution heat treatment of a third-generation Ni-based single crystal superalloy. *International Journal of Fatigue* 130, 105247. <https://doi.org/10.1016/j.ijfatigue.2019.105247>
- Byun, T., Hashimoto, N., Farrell, K., 2004. Temperature dependence of strain hardening and plastic instability behaviors in austenitic stainless steels. *Acta Materialia* 52, 3889–3899. <https://doi.org/10.1016/j.actamat.2004.05.003>
- Charkaluk, E., Constantinescu, A., 2009. Dissipative aspects in high cycle fatigue. *Mechanics of Materials* 41, 483–494. <https://doi.org/10.1016/j.mechmat.2009.01.018>
- Christ, H., Grigorescu, A., Müller-bollenhagen, C., Zimmermann, M., 2015. Metastable Austenitic Stainless Steels and the Effect of Deformation-Induced Phase Transformation on the Fatigue Properties, Siegen.
- Colin, J., Fatemi, A., Taheri, S., 2010. Fatigue Behavior of Stainless Steel 304L Including Strain

- Hardening, Prestraining, and Mean Stress Effects. *Journal of Engineering Materials and Technology* 132, 021008. <https://doi.org/10.1115/1.4000224>
- Das, A., Sivaprasad, S., Ghosh, M., Chakraborti, P.C., Tarafder, S., 2008. Morphologies and characteristics of deformation induced martensite during tensile deformation of 304 LN stainless steel. *Materials Science and Engineering: A* 486, 283–286. <https://doi.org/10.1016/j.msea.2007.09.005>
- De, A.K., Speer, J.G., Matlock, D.K., Murdock, D.C., Mataya, M.C., Comstock, R.J., 2006. Deformation-induced phase transformation and strain hardening in type 304 austenitic stainless steel. *Metallurgical and Materials Transactions A* 37, 1875–1886. <https://doi.org/10.1007/s11661-006-0130-y>
- Dengel, D., Harig, H., 1980. Estimation of the fatigue limit by progressively-increasing load tests. *Fatigue & Fracture of Engineering Materials and Structures* 3, 113–128. <https://doi.org/10.1111/j.1460-2695.1980.tb01108.x>
- Desu, R.K., Nitin Krishnamurthy, H., Balu, A., Gupta, A.K., Singh, S.K., 2016. Mechanical properties of Austenitic Stainless Steel 304L and 316L at elevated temperatures. *Journal of Materials Research and Technology* 5, 13–20. <https://doi.org/10.1016/j.jmrt.2015.04.001>
- Doudard, C., Calloch, S., 2009. Influence of hardening type on self-heating of metallic materials under cyclic loadings at low amplitude. *European Journal of Mechanics - A/Solids* 28, 233–240. <https://doi.org/10.1016/j.euromechsol.2008.08.002>
- Doudard, C., Calloch, S., Cugy, P., Galtier, A., Hild, F., 2005. A probabilistic two-scale model for high-cycle fatigue life predictions. *Fatigue & Fracture of Engineering Materials & Structures* 28, 279–288. <https://doi.org/10.1111/j.1460-2695.2005.00854.x>
- Doudard, C., Calloch, S., Hild, F., Roux, S., 2010. Identification of heat source fields from infrared thermography: Determination of ‘self-heating’ in a dual-phase steel by using a dog bone sample. *Mechanics of Materials* 42, 55–62. <https://doi.org/10.1016/j.mechmat.2009.09.005>
- Ezanno, A., Doudard, C., Calloch, S., Heuzé, J.-L., 2013. A new approach to characterizing and modeling the high cycle fatigue properties of cast materials based on self-heating measurements under cyclic loadings. *International Journal of Fatigue* 47, 232–243. <https://doi.org/10.1016/j.ijfatigue.2012.09.005>
- Grigorescu, A.C., Hilgendorff, P.M., Zimmermann, M., Fritzen, C.P., Christ, H.J., 2016. Cyclic deformation behavior of austenitic Cr–Ni-steels in the VHCF regime: Part I – Experimental study. *International Journal of Fatigue* 93, 250–260. <https://doi.org/10.1016/j.ijfatigue.2016.05.005>
- Gupta, S., Kucharczyk, P., Münstermann, S., Jayaganthan, R., 2018. Prestraining Induced Enhancement in the Fatigue Limit Obtained by Load Increasing Thermal Method for Metastable Austenitic Stainless Steel. *steel research international* 89. <https://doi.org/10.1002/srin.201700434>
- Hahnenberger, F., Smaga, M., Eifler, D., 2014. Microstructural investigation of the fatigue behavior and phase transformation in metastable austenitic steels at ambient and lower temperatures. *International Journal of Fatigue* 69, 36–48. <https://doi.org/10.1016/j.ijfatigue.2012.07.004>
- Hahnenberger, F., Smaga, M., Eifler, D., 2012. Influence of  $\gamma$ - $\alpha'$ -Phase Transformation in Metastable Austenitic Steels on the Mechanical Behavior During Tensile and Fatigue Loading at Ambient and Lower Temperatures. *Advanced Engineering Materials* 14, 853–858. <https://doi.org/10.1002/adem.201100341>
- Haušild, P., Davydov, V., Drahokoupil, J., Landa, M., Pilvin, P., 2010. Characterization of strain-induced

- martensitic transformation in a metastable austenitic stainless steel. *Materials & Design* 31, 1821–1827. <https://doi.org/10.1016/j.matdes.2009.11.008>
- Hecker, S.S., Stout, M.G., Staudhammer, K.P., Smith, J.L., 1982. Effects of Strain State and Strain Rate on Deformation-Induced Transformation in 304 Stainless Steel: Part I. Magnetic Measurements and Mechanical Behavior. *Metallurgical Transactions A* 13, 619–626. <https://doi.org/10.1007/BF02644427>
- Hedström, P., Lindgren, L.E., Almer, J., Lienert, U., Bernier, J., Terner, M., Odén, M., 2009. Load Partitioning and Strain-Induced Martensite Formation during Tensile Loading of a Metastable Austenitic Stainless Steel. *Metallurgical and Materials Transactions A* 40, 1039–1048. <https://doi.org/10.1007/s11661-009-9807-3>
- Kamaya, M., Kawakubo, M., 2015. Mean stress effect on fatigue strength of stainless steel. *International Journal of Fatigue* 74, 20–29. <https://doi.org/10.1016/j.ijfatigue.2014.12.006>
- Kaoumi, D., Liu, J., 2018. Deformation induced martensitic transformation in 304 austenitic stainless steel: In-situ vs. ex-situ transmission electron microscopy characterization. *Materials Science and Engineering: A* 715, 73–82. <https://doi.org/10.1016/j.msea.2017.12.036>
- Krapez, J.-C., Pacou, D., 2002. Thermography detection of early thermal effects during fatigue tests of steel and aluminum samples, in: *AIP Conference Proceedings*. AIP. <https://doi.org/10.1063/1.1472977>
- Krapez, J.-C., Pacou, D., Gardette, G., 2000. Lock-in thermography and fatigue limit of metals, in: *Proceedings of the 2000 International Conference on Quantitative InfraRed Thermography*. QIRT Council. <https://doi.org/10.21611/qirt.2000.051>
- Krupp, U., West, C., Christ, H.-J., 2008. Deformation-induced martensite formation during cyclic deformation of metastable austenitic steel: Influence of temperature and carbon content. *Materials Science and Engineering: A* 481–482, 713–717. <https://doi.org/10.1016/j.msea.2006.12.211>
- Le Roux, J.-C., Taheri, S., Sermage, J.-P., Colin, J., Fatemi, A., 2008. Cyclic Deformation and Fatigue Behaviors of Stainless Steel 304L Including Mean Stress and Pre-Straining Effects, in: *Volume 3: Design and Analysis*. ASMEDC, pp. 411–420. <https://doi.org/10.1115/PVP2008-61789>
- Liu, J., Deng, X.T., Huang, L., Wang, Z.D., 2018. High-cycle fatigue behavior of 18Cr-8Ni austenitic stainless steels with grains ranging from nano/ultrafine-size to coarse. *Materials Science and Engineering: A* 733, 128–136. <https://doi.org/10.1016/j.msea.2018.07.043>
- Liu, J., Kaoumi, D., 2018. Use of in-situ TEM to characterize the deformation-induced martensitic transformation in 304 stainless steel at cryogenic temperature. *Materials Characterization* 136, 331–336. <https://doi.org/10.1016/j.matchar.2017.12.005>
- Louge, J., 2019. Apports des mesures d'auto-échauffement pour l'étude de la fatigue des aciers : effets d'histoire et cisaillement. PhD Thesis, ENSTA Bretagne, France.
- Masquelier, I., Marco, Y., Le Saux, V., Calloch, S., Charrier, P., 2015. Determination of dissipated energy fields from temperature mappings on a rubber-like structural sample: Experiments and comparison to numerical simulations. *Mechanics of Materials* 80, 113–123. <https://doi.org/10.1016/j.mechmat.2014.09.010>
- Meneghetti, G., Ricotta, M., Atzori, B., 2016. A two-parameter, heat energy-based approach to analyse the mean stress influence on axial fatigue behaviour of plain steel specimens. *International Journal of Fatigue* 82, 60–70. <https://doi.org/10.1016/j.ijfatigue.2015.07.028>

- Mostofizadeh, P., Kadkhodaei, M., Arbab Chirani, S., Saint-Sulpice, L., Rokbani, M., Bouraoui, T., Calloch, S., 2019. Fatigue analysis of shape memory alloys by self-heating method. *International Journal of Mechanical Sciences* 156, 329–341. <https://doi.org/10.1016/j.ijmecsci.2019.04.012>
- Müller-Bollenhagen, C., Zimmermann, M., Christ, H.-J., 2010a. Adjusting the very high cycle fatigue properties of a metastable austenitic stainless steel by means of the martensite content. *Procedia Engineering* 2, 1663–1672. <https://doi.org/10.1016/j.proeng.2010.03.179>
- Müller-Bollenhagen, C., Zimmermann, M., Christ, H.-J., 2010b. Very high cycle fatigue behaviour of austenitic stainless steel and the effect of strain-induced martensite. *International Journal of Fatigue* 32, 936–942. <https://doi.org/10.1016/j.ijfatigue.2009.05.007>
- Munier, R., Doudard, C., Calloch, S., Weber, B., 2017. Identification of the micro-plasticity mechanisms at the origin of self-heating under cyclic loading with low stress amplitude. *International Journal of Fatigue* 103, 122–135. <https://doi.org/10.1016/j.ijfatigue.2017.05.027>
- Munier, R., Doudard, C., Calloch, S., Weber, B., 2014. Determination of high cycle fatigue properties of a wide range of steel sheet grades from self-heating measurements. *International Journal of Fatigue* 63, 46–61. <https://doi.org/10.1016/j.ijfatigue.2014.01.004>
- Munier, R., Doudard, C., Calloch, S., Weber, B., 2010. Towards a faster determination of high cycle fatigue properties taking into account the influence of a plastic pre-strain from selfheating measurements. *Procedia Engineering* 2, 1741–1750. <https://doi.org/10.1016/j.proeng.2010.03.187>
- Nakajima, M., Jung, J.W., Uematsu, Y., Tokaji, K., 2007. Coaxing Effect in Stainless Steels and High-Strength Steels. *Key Engineering Materials* 345–346, 235–238. <https://doi.org/10.4028/www.scientific.net/KEM.345-346.235>
- Olson, G.B., Cohen, M., 1972. A mechanism for the strain-induced nucleation of martensitic transformations. *Journal of the Less Common Metals* 28, 107–118. [https://doi.org/10.1016/0022-5088\(72\)90173-7](https://doi.org/10.1016/0022-5088(72)90173-7)
- Paquet, D., Lantaigne, J., Bernard, M., Baillargeon, C., 2014. Characterizing the effect of residual stresses on high cycle fatigue (HCF) with induction heating treated stainless steel specimens. *International Journal of Fatigue* 59, 90–101. <https://doi.org/10.1016/j.ijfatigue.2013.09.011>
- Pessoa, D.F., Kirchhoff, G., Zimmermann, M., 2017. Influence of loading frequency and role of surface micro-defects on fatigue behavior of metastable austenitic stainless steel AISI 304. *International Journal of Fatigue* 103, 48–59. <https://doi.org/10.1016/j.ijfatigue.2017.05.018>
- Puget, M., 2013. Influence du procédé sur la tenue à la fatigue des pièces forgées : application à une tige fémorale. PhD thesis, l'Université de Bretagne Occidentale, France.
- Ricotta, M., Meneghetti, G., Atzori, B., Risitano, G., Risitano, A., 2019. Comparison of Experimental Thermal Methods for the Fatigue Limit Evaluation of a Stainless Steel. *Metals* 9, 1–23. <https://doi.org/10.3390/met9060677>
- Risitano, A., Risitano, G., 2013. Determining fatigue limits with thermal analysis of static traction tests. *Fatigue & Fracture of Engineering Materials & Structures* 36, 631–639. <https://doi.org/10.1111/ffe.12030>
- Roué, V., Doudard, C., Calloch, S., Montel, F., Pujol D'Andrebo, Q., Corpacce, F., 2018. Rapid determination of the high cycle fatigue properties of high temperature aeronautical alloys by self-heating measurements. *MATEC Web of Conferences*. <https://doi.org/10.1051/mateconf/201816522022>

- Saint-Sulpice, L., Lakrit, M., Arbab Chirani, S., Calloch, S., 2014. Variation in electric resistivity in metastable alloys during thermomechanical loading: Effects of temperature, elasticity, plasticity and phase transformation. *Mechanics of Materials* 71, 1–9. <https://doi.org/10.1016/j.mechmat.2014.01.004>
- Schramm, R.E., Reed, R.P., 1975. Stacking fault energies of seven commercial austenitic stainless steels. *Metallurgical Transactions A* 6, 1345–1351. <https://doi.org/10.1007/BF02641927>
- Shen, Y.F., Li, X.X., Sun, X., Wang, Y.D., Zuo, L., 2012. Twinning and martensite in a 304 austenitic stainless steel. *Materials Science and Engineering: A* 552, 514–522. <https://doi.org/10.1016/j.msea.2012.05.080>
- Smaga, M., Walther, F., Eifler, D., 2006. Investigation and modelling of the plasticity-induced martensite formation in metastable austenites. *International Journal of Materials Research* 97, 1648–1655. <https://doi.org/10.3139/146.101396>
- Sugimoto, K.-I., 2009. Fracture strength and toughness of ultra high strength TRIP aided steels. *Materials Science and Technology* 25, 1108–1117. <https://doi.org/10.1179/174328409X453307>
- Talonen, J., 2007. Effect of strain-induced  $\alpha'$ -martensite transformation on mechanical properties of metastable austenitic stainless steels. Helsinki University of Technology. PhD thesis, Helsinki University of Technology, Finland.
- Talonen, J., Aspegren, P., Hänninen, H., 2004. Comparison of different methods for measuring strain induced  $\alpha$ -martensite content in austenitic steels. *Materials Science and Technology* 20, 1506–1512. <https://doi.org/10.1179/026708304X4367>
- Talonen, J., Hänninen, H., 2007. Formation of shear bands and strain-induced martensite during plastic deformation of metastable austenitic stainless steels. *Acta Materialia* 55, 6108–6118. <https://doi.org/10.1016/j.actamat.2007.07.015>
- Talonen, J., Hänninen, H., Nenonen, P., Pape, G., 2005. Effect of strain rate on the strain-induced  $\gamma \rightarrow \alpha'$ -martensite transformation and mechanical properties of austenitic stainless steels. *Metallurgical and Materials Transactions A* 36, 421–432. <https://doi.org/10.1007/s11661-005-0313-y>
- Torabian, N., Favier, V., Dirrenberger, J., Adamski, F., Ziaei-Rad, S., Ranc, N., 2017. Correlation of the high and very high cycle fatigue response of ferrite based steels with strain rate-temperature conditions. *Acta Materialia* 134, 40–52. <https://doi.org/10.1016/j.actamat.2017.05.064>
- Vincent, L., Le Roux, J.C., Taheri, S., 2012. On the high cycle fatigue behavior of a type 304L stainless steel at room temperature. *International Journal of Fatigue* 38, 84–91. <https://doi.org/10.1016/j.ijfatigue.2011.11.010>
- Wan, J., Chen, S., Xu, Z., 2001. The influence of temperature on stacking fault energy in Fe-based alloys. *Science in China Series E: Technological Sciences* 44, 345–352. <https://doi.org/10.1007/BF02916685>
- Wu, Z., Huang, Y., 2015. Characterization of a Metastable Austenitic Stainless Steel with Severe Plastic Distortions. *Procedia Engineering* 99, 1323–1329. <https://doi.org/10.1016/j.proeng.2014.12.666>
- Zeng, W., Yuan, H., 2017. Mechanical behavior and fatigue performance of austenitic stainless steel under consideration of martensitic phase transformation. *Materials Science and Engineering: A* 679, 249–257. <https://doi.org/10.1016/j.msea.2016.10.005>
- Zhang, L., Liu, X.S., Wu, S.H., Ma, Z.Q., Fang, H.Y., 2013. Rapid determination of fatigue life based on temperature evolution. *International Journal of Fatigue* 54, 1–6.

<https://doi.org/10.1016/j.ijfatigue.2013.04.002>

Zheng, C., Yu, W., 2018. Effect of low-temperature on mechanical behavior for an AISI 304 austenitic stainless steel. *Materials Science and Engineering: A* 710, 359–365.  
<https://doi.org/10.1016/j.msea.2017.11.003>